Influence of infill properties on flexural rigidity of 3D-printed structural members

J. H. Porter[a], T. M. Cain[b], S. L. Fox[a], P. S. Harvey Jr.[b,*]

[a]*School of Aerospace and Mechanical Engineering, University of Oklahoma, Norman, OK 73019, USA*
[b]*School of Civil Engineering and Environmental Science, University of Oklahoma, Norman, OK 73019, USA*

Abstract

This paper characterizes the flexural properties of relatively slender structural members (beams) manufactured using a FDM-based 3D printer. The primary goal is to assess the influence of infill properties on flexural rigidity through a parametric investigation. Infill percentage, infill orientation, and member thickness provided the parametric variation. The beams were tested by three-point bending, free vibration, and buckling. The tests showed that flexural rigidity varied linearly with infill percentage over most of the range considered, but fell off quickly below 10% infill. The optimal infill percentage that maximized specific flexural rigidity (flexural rigidity to length density) of the beams was determined to be between 10% and 20%.

Keywords: flexural rigidity, infill, FDM, PLA, 3D printing

1. Introduction

Aerospace and automotive industries seek to minimize weight while maintaining strength. Engineers design structural members to efficiently use materials, such as in wide flange beams and iso- and ortho-grid stiffened panels. Cellular structures attainable via additive manufacturing (or 3D printing) present a way to minimize the use of material and achieve a high strength-to-weight ratio [1]. 3D printing provides an opportunity to reduce weight with

*Corresponding author. Address: School of Civil Engineering and Environmental Science, University of Oklahoma, 202 W. Boyd St., Norman, OK 73019-1024, USA. Tel.: +1 405 325 3836
Email address: harvey@ou.edu (P. S. Harvey Jr.)

smaller losses in strength (or stiffness) by tailoring the internal matrix [2]. In recent years, 3D printers have become widely available, expanding the opportunities to use 3D-printed parts in a variety of applications [3, 4]. For example, custom orthoses and prostheses provide one such opportunity for extensive use of additive manufacturing processes [5, 6]. The motivation of this paper arises from the need to better understand the capabilities (and limitations) of 3D printing to fabricate structural members subject to *flexure* (e.g., unmanned aerial vehicle components [7]). As such, the (elastic) flexural properties and structural efficiency of 3D-printed members are of interest. In this study, the characterization and assessment of the effect of infill properties (percentage and orientation) on the flexural properties of polylactic acid (PLA) specimens manufactured with fused deposition modelling (FDM) technique are examined. A background on related studies seeking to characterize mechanical properties of 3D-printed parts is presented below. Additional background is available in Refs. [8, 9, 10].

Most previous studies that characterize 3D-printed specimens focused on tensile testing [10]. Zhou et al. [11] examined the ultimate tensile strength and the modulus of elasticity for different infill densities and patterns. They concluded that 20% infill with a triangular pattern had the highest strength to weight for the tested infill percentages of 20%, 50%, and 80%. Gurrala and Regalla [12] studied the impact of infill density and print directions on ultimate tensile strength and volumetric shrinkage. They found that optimal strength occured at the highest infill density, and that the print directions for optimal strength and volumetric shrinkage were different. Smith and Dean [13] investigated the tensile elastic modulus and ultimate tensile strength of solid 3D-printed specimens. They found that tensile properties depended on print orientation and were 30% to 53% weaker than published bulk material properties. Wittbrodt and Pearce [14] examined the ultimate tensile strength for different colors and print temperatures of PLA. They concluded that material color does effect tensile strength and that care must be taken to select the optimal print temperature for each color [14]. Chacón et al. [15] studied the impact of build orientation, layer thickness, and feed rate on tensile properties, as well as bending properties. They saw significant differences in tensile and flexural strengths and concluded that build orientation and layer thickness both have a significant impact on tensile and flexural strength [15].

Tensile tests of 3D-printed specimens do not transfer well to flexural properties, so recent studies have focused specifically on flexural testing. Virgin [16] examined the flexural properties of 3D-printed specimens with respect to print orientations and density settings. He used three-point bending, free vibration and buckling tests to determine the flexural modulus of each specimens. The lower density settings showed decreased flexural modulus values. Virgin also notes that print orientation can effect the flexural modulus by up to 25% with the on-edge orientation being the strongest [16]. Other studies have also concluded that specimens printed on-edge demonstrate better mechanical properties [15, 17]. Lužanin et al. [3] examined the maximum "flexural force" (the lateral force applied to a flexural member) for various layer thicknesses, deposition angles, and infill percentage. They concluded that layer thickness has the largest impact on ultimate flexural force. Motaparti et al. [17] investigated the impact of other printer settings such as raster angle and air gap on flexural properties. They found that negative air gaps between layers increased flexural yield strength and that flexural yield strength varied with raster angle [17].

While the above mentioned studies sought to characterize the influence of various printing parameters (e.g., build orientation, layer thickness, raster angle) on the mechanical properties of 3D-printed parts, a major focus of this study is on infill percentage. As previously mentioned, Lužanin et al. [3] examined the influence of infill percentage, determining that the impact of infill percentage over the range of 10 to 30% was not statistically significant. However, they did not examine flexural rigidity in the elastic range or over the full range of possible infill percentages. Alvarez et al. [18] investigated the effect of infill percentage on tensile strength and impact resistance, showing that higher infill percentage resulted in better (greater) strength at the expense of increased print time.

This study aims to determine the most efficient infill properties for 3D-printed flexible structural members [19, 20]. The main emphasis is to characterize the effect of infill percentage on elastic flexural behavior (in terms of flexural rigidity, EI) taking into account the weight of the fabricated specimens (in terms of mass per unit length, m). The flexural rigidity, EI, of the specimens was determined through three-point bending and free vibration tests, with buckling tests for comparison and confirmation. The results are presented

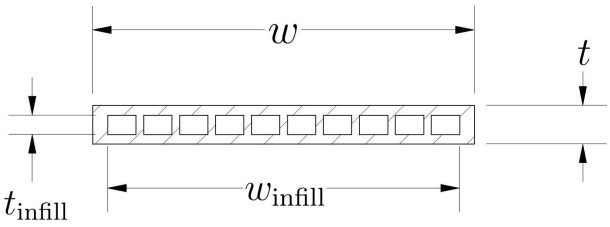

Figure 1: Beam cross section dimensions.

in terms of specific flexural rigidity, EI/m, to quantify the efficiency (stiffness-to-mass) of each infill design. While a direct comparison of theory and experiment relies on accurate measurements and appropriate values of geometrical and material properties, the important concept developed is how flexural properties are influenced by changes in infill properties in a *comparative* sense.

2. Theoretical background

2.1. Flexural rigidity and infill percentage

The flexural rigidity of a beam is a function of the second moment of area (I) and the elastic modulus (E). For the theoretical model, the elastic modulus is assumed to be constant. The second moment of area of the beam is a function of infill percentage (p), size (width w and thickness t), and the dimensions of the non-solid interior ($w_{\text{infill}} \times t_{\text{infill}}$); see Fig. 1. The specimens were tested about their weak axis perpendicular to the z-axis of the print orientation. The printer settings (Section 3.1) were chosen such that the cross section was symmetric. At any given cross section, a smeared (infill) stiffener technique [21] is assumed such that the center portion has approximately the infill percentage worth of area, i.e., $p\, w_{\text{infill}}\, t_{\text{infill}}$. The infill generally consists of one pattern through the thickness (from top to bottom) of the central cavity and therefore affects only the linear (width) term in the second moment of area, but not the cubic (thickness) term. The second moment of area of the composite cross section (shell + smeared infill) is given by

$$I = I_{\text{shell}} + I_{\text{infill}} = \left(\frac{wt^3}{12} - \frac{w_{\text{infill}} t_{\text{infill}}^3}{12} \right) + \frac{p w_{\text{infill}} t_{\text{infill}}^3}{12} \equiv \frac{wt^3}{12} - (1-p) \frac{w_{\text{infill}} t_{\text{infill}}^3}{12} \qquad (1)$$

From this equation, it can be seen that I depends linearly on the infill percentage p. The flexural rigidity of the beam is given by

$$EI = E\frac{wt^3}{12} - (1-p)E\frac{w_{\text{infill}}t_{\text{infill}}^3}{12} \tag{2}$$

The theoretical mass per unit length, denoted m, also scales linearly with the infill percentage:

$$m = \rho[wt - (1-p)w_{\text{infill}}t_{\text{infill}}] \tag{3}$$

where ρ is the material density. The *specific flexural rigidity* is defined as the ratio of the flexural rigidity to the mass per unit length, or

$$\frac{EI}{m} = \frac{Et^2}{12\rho}\left[\frac{1-(1-p)(w_{\text{infill}}/w)(t_{\text{infill}}/t)^3}{1-(1-p)(w_{\text{infill}}/w)(t_{\text{infill}}/t)}\right] \tag{4}$$

This expression is used in subsequent sections to quantify the stiffness-to-weight of the cross section under varying infill percentage.

Consider the two limiting cases: $p = 1$ (solid) and 0 (hollow). For the solid case, the specific flexural rigidity is

$$\left.\frac{EI}{m}\right|_{p=1} = \frac{Et^2}{12\rho}$$

which is independent of the width of the beam because both EI and m grow linearly in w for a solid beam. For the hollow case, the specific flexural rigidity is

$$\left.\frac{EI}{m}\right|_{p=0} = \frac{Et^2}{12\rho}\left[\frac{1-(w_{\text{infill}}/w)(t_{\text{infill}}/t)^3}{1-(w_{\text{infill}}/w)(t_{\text{infill}}/t)}\right]$$

The term in brackets is greater than or equal to unity for applicable ranges of w_{infill}/w and t_{infill}/t, i.e., $\in (0, 1]$. Therefore, it is advantageous in terms of specific flexural rigidity to use a hollow section ($w_{\text{infill}} = 0$ or $t_{\text{infill}} = 0$). Furthermore, for $0 < p < 1$ the specific flexural rigidity is bounded from above by $(EI/m)|_{p=0}$ and from below by $(EI/m)|_{p=1}$, monotonically decreasing therebetween, as shown later.

The flexural properties defined above play a key role in the three test methods used in the experimental portion of the study—three-point bending, free vibration, and buckling—as described here.

2.2. Three-point bending

The maximum deflection of the center of a simply-supported beam under a mid-span point load F is given by

$$\Delta_{\max} = \frac{F L_{\text{span}}^3}{48 EI} \tag{5}$$

where L_{span} is the span length of the beam. The maximum deflection depends on the flexural rigidity EI of the beam, but not mass per unit length, m, because the load F is applied (quasi-)statically.

2.3. Free Vibration

The natural vibratory frequencies of a cantilevered beam can be determined based on the geometry and material properties of the beam. The fundamental frequency of the beam (in Hz) is given by [22]

$$f_1 = \frac{1.875^2}{(2\pi) L_{\text{free}}^2} \sqrt{\frac{EI}{m}} \tag{6}$$

where L_{free} is the free length of the beam, and the term under the radical is the specific flexural rigidity. This equation assumes a perfectly clamped end and uniform EI/m over the free the length of the specimen.

2.4. Buckling

The critical buckling load of an axially loaded strut is given by Euler's formula:

$$P_{\text{cr}} = \frac{\pi^2 EI}{(KL)^2} \tag{7}$$

where L is the total (unsupported) length of the strut and K is the column effective length factor. The simplest (Euler) buckling case corresponds to pinned boundary conditions, for which $K = 1$. Note that Euler's formula (Eq. (7)) assumes a perfectly flat strut with no load eccentricity, which is difficult, if not impossible, to achieve experimentally. Like three-point bending, the critical buckling load depends on EI, but not m.

3. Materials and methods

3.1. Test specimen design and fabrication

The aim of this study is to analyze the influence of the infill percentage and infill orientation on the flexural properties of 3D-printed parts. The test specimens were designed to be used in all three test procedures. They were therefore designed to be quite flexible with nominal dimensions of $L = 177.8$ mm, $w = 25.4$ mm, and $t = 2.55$ mm (*thin*) or 3.825 mm (*thick*). The selection of these thicknesses is discussed below. The test specimens were printed out of PolyLite PLA [23] with a consumer grade FDM printer (Taz 6, LulzBot, Loveland, CO). G-codes to control the process of fabricating the parts were generated in the accompanying software (Cura LulzBot Edition, v2.6.66) from Stereo lithography (STL) files.

The test specimens were manufactured with varying infill percentage and infill orientation, while keeping the other printing parameters constant (see Table 1). The specimen thicknesses were chosen to maintain symmetry of the cross section; i.e., so that the solid bottom and top layers had the same nominal thickness (0.6375 mm). Printing specimens with a smaller bottom layer height showed a lower quality surface finish on the bottom, so the manufacturer's recommended value (0.425 mm) was used. Specimens were printed individually in identical orientations at the same location on the bed of the printer.

The main parameter of interest was the infill percentage of the beams. Infill percentages of 0, 5, 10, 15, 20, 30, 50, 70, and 100 % were considered for the thin beam, whereas, for

Table 1: Values of the fixed print parameters.

Parameter, units	Value	Parameter, units	Value
Layer height, mm	0.2125	Bed temperature, °C	60
Initial layer height, mm	0.4250	Nozzle temperature, °C	205
Solid bottom layers	2	Nozzle size, mm	0.5
Solid top layers	3	Material diameter, mm	2.85
Line width, mm	0.5	Infill pattern	grid

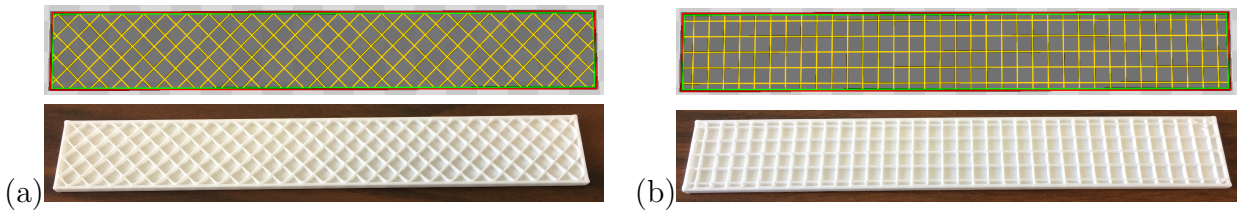

Figure 2: Infill orientations: (a) $+45°/-45°$ and (b) $0°/90°$.

the thick beam, infill percentages were considered only between 0 and 30 %. This reduced range of infill densities was selected to adequately resolve the optimal infill density in terms of specific flexural rigidity (Section 4.3). The specimens were printed with a *grid* infill pattern (the default infill pattern in Cura, as well as many other printers, e.g., MakerBot and Stratasys). Additional tests were conducted with the thin beam using the solid setting as opposed to 100 % infill and with infill percentages of 15, 20, and 30 with a different infill orientation (see Fig. 2). The default infill orientation for the printer is $+45°/-45°$. An infill orientation of $0°/90°$ was tested as an alternative.

The full test matrix is shown in Table 2. Specimen 3 serves as the *baseline case*, as it was fabricated with the default infill properties. Five test specimens were printed for this baseline case (later to be identified as 3, 3b, 3c, 3d, and 3e), whereas only one of each of the other specimens was printed.

The dimensions of the fabricated specimens were measured to compare the experimental results to the theoretical model. All of the specimens were an average of 0.3 mm thicker than the nominal value. This is equivalent to a 12% increase for the thinner beams and 8% for the thicker beams. Across all of the specimens, the width and length were on average 0.5% larger than the nominal values.

For the PLA used, the manufacturer lists the Young's modulus and bending modulus as 2.636 ± 0.330 and 3.283 ± 0.132 GPa, respectively [23]. The published bending modulus (3.283 GPa) was used for calculating the theoretical flexural rigidity and specific flexural rigidity presented in Section 4.

3.2. Test Methodologies

3.2.1. Three-point bending tests

The lateral stiffnesses of the test specimens were determined using three-point bending tests [24]. The test setup is shown in Fig. 3(a). Each specimen was centered on a 3D-printed loading apparatus comprised of lower supports and a loading nose midway between the

Table 2: Test specimens. Specimen 3 is the baseline case; specimen 8 was printed solid; specimens 1–14 were printed prior to printing specimens 15–19.

Specimen	Infill properties		Nominal
No.	Percentage (%)	Orientation	thickness (mm)
1	10	+45°/−45°	2.550
2	15	+45°/−45°	2.550
3	**20**	**+45°/−45°**	**2.550**
4	30	+45°/−45°	2.550
5	50	+45°/−45°	2.550
6	70	+45°/−45°	2.550
7	100	+45°/−45°	2.550
8	–	–	2.550
9	15	+45°/−45°	3.825
10	20	+45°/−45°	3.825
11	30	+45°/−45°	3.825
12	15	0°/90°	2.550
13	20	0°/90°	2.550
14	30	0°/90°	2.550
15	5	+45°/−45°	2.550
16	5	+45°/−45°	3.825
17	0	+45°/−45°	2.550
18	0	+45°/−45°	3.825
19	10	+45°/−45°	3.825

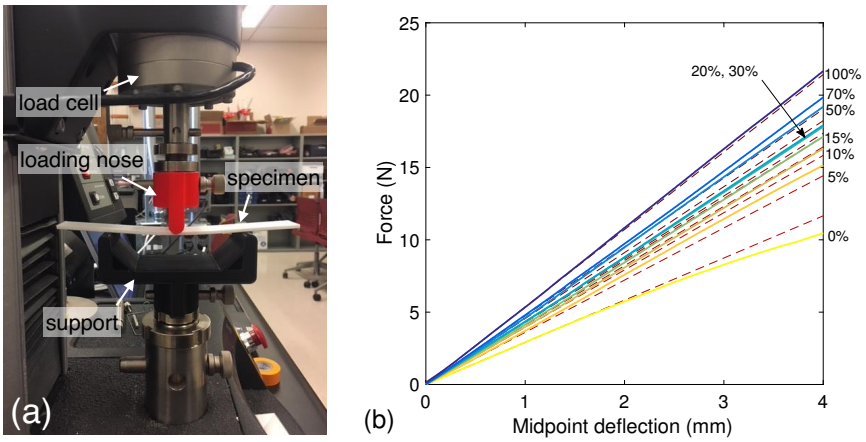

Figure 3: (a) Photograph of three-point bending test setup. (b) Representative force-deflection relations for thin specimens with varying infill percentages in orientation 1; $+45°/-45°$ infill orientation.

supports. The same PLA that was used for the specimens was used for the loading apparatus, which was designed to be sufficiently rigid (compared to the flexible specimens) to ensure the load-deflection data was not affected. The supports and nose had cylindrical surfaces with radii of 5 mm. The support span (L_{span}) was 101.6 mm. The apparatus was incorporated into an Universal Testing Machine (5543, Instron, Norwood, MA), which applied a gradual load through the loading nose. The resulting deflection of the specimen at its midpoint was recorded throughout each test. Each specimen was deflected at a rate of 0.1667 mm/s for a total deflection of 5 mm. Each specimen was tested twice, once in the upwards facing position (orientation 1) and once in the downwards facing position (orientation 2). Representative force-deflection curves are shown in Fig. 3(b) for the thin specimens (17, 15, and 1–7) in orientation 1. The slope of the force-deflection curve gives the effective lateral stiffness, $48EI/L_{\text{span}}$ (see Eq. (5)), which was used to determine the flexural rigidity EI. Eq. (5) assumes small deflections, so the slope of the force-deflection curve was fitted using a straight line over the first 0.4 mm of deflection. The fitted lines are shown in Fig. 3(b) by the dashed lines. Fitting to the small deflection region ensures that nonlinearities associated with "large deflection" do not artificially raise or lower the experimentally determined flexural rigidity; see for example the reduction in stiffness (softening) in the 0% infill case.

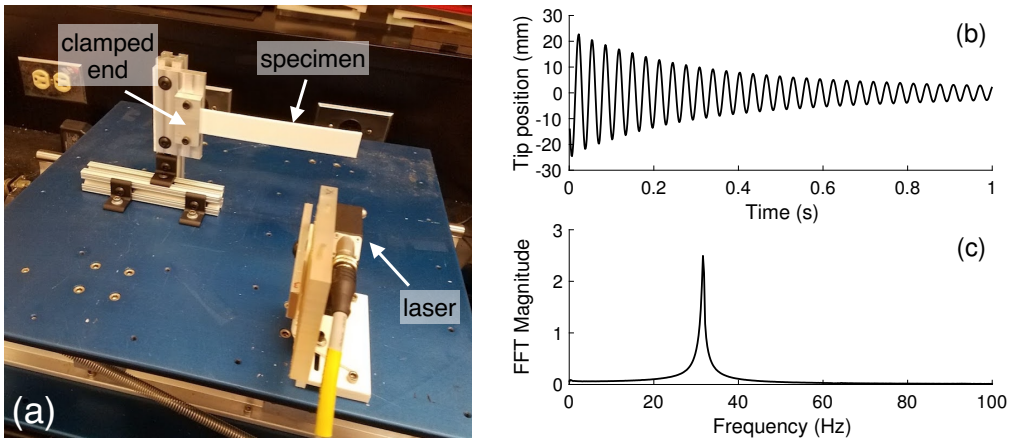

Figure 4: (a) Photograph of free vibration test setup. Representative free vibration time series (b) and fast Fourier transform (c) for specimen 3.

3.2.2. Free vibration tests

The natural frequencies of the test specimens were determined using the free vibration of a cantilevered beam [25] (see Fig. 4(a)). A laser (ILD1302-200, Micro Epsilon, Ortenburg, Germany) was used to measure the position of the beam at 750 samples per second. The clamped length of the beam was 25.4 mm, so the free length of the beam (L_{free}) was 152.4 mm. The beams were initially displaced at their tips and then released, and the free vibration data was recorded. The beams were very lightly damped, so the natural frequency was not significantly impacted by damping. Fig. 4(b) shows a typical time series from a test of specimen 3. To determine the fundamental natural frequency f_1, the fast Fourier transform (FFT) of the time series was calculated. Fig. 4(c) shows the FFT of the representative time series (Fig. 4(b)). The vibrations of the beams died out quickly limiting the resolution of the FFT. A Gaussian function was used to interpolate the FFT in close proximity to the peaks to improve resolution and to more accurately determine the fundamental frequency [26]. Each beam was tested at least twice, once with each end clamped. Once the natural frequency was determined, Eq. (6) was used to calculate the specific flexural rigidity. To determine the flexural rigidity, the specific flexural rigidity was multiplied by the length density, which was determined by dividing the measured (total) mass by the nominal length.

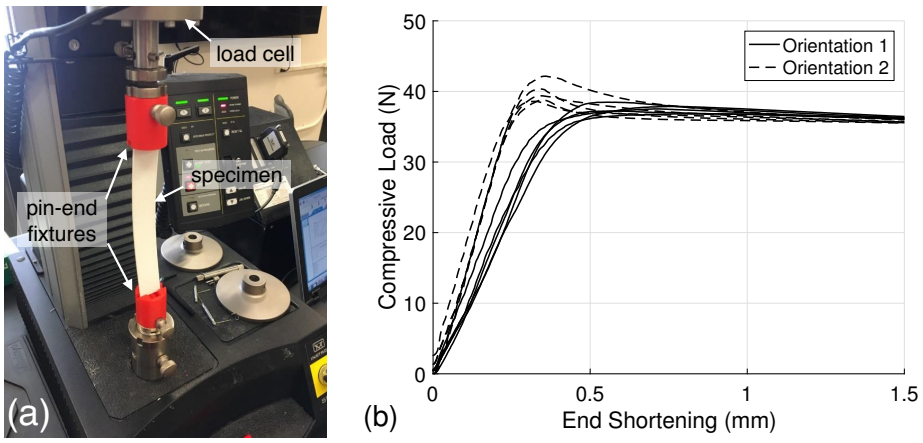

Figure 5: (a) Photograph of buckling test setup. (b) Representative compressive load versus end shortening (axial deflection) relations for specimen 3.

3.3. Buckling tests

Buckling tests were used to confirm the results of the three-point bending and free vibration tests rather than directly characterize the flexural properties of the specimens. The method of this investigation followed generally the simple buckling test procedure by Virgin [16]. The test setup is shown in Fig. 5(a). The same universal testing machine that was used for the three-point bending tests was used for the buckling tests. To approximate Euler buckling and allow the entire length of the specimen to buckle, custom fixtures (pictured in Fig. 5(a)) were designed and 3D printed. The fixtures were designed to approximate frictionless pin connections. These load fixtures were attached to the load frame using clevis pins and were aligned to reduce load eccentricities.

Each specimen was set into the load fixture, and the load head was brought to just contact the specimen with a sufficiently small load ($\leqslant$ 5 N) to hold the specimen in the test apparatus. The load test was then initiated using a constant displacement rate of 0.05 mm/s until a displacement of 1.5 mm was reached. The applied load and corresponding end shortening (axial deflection) were collected; representative compressive load-end shortening curves are shown in Fig. 5(b). Each specimen was tested a second time in an inverted orientation. The axial load measured at an end shortening of 1.5 mm (approximately 0.84% axial strain) was used to estimate the buckling load P_{cr}. These experimentally measured buckling

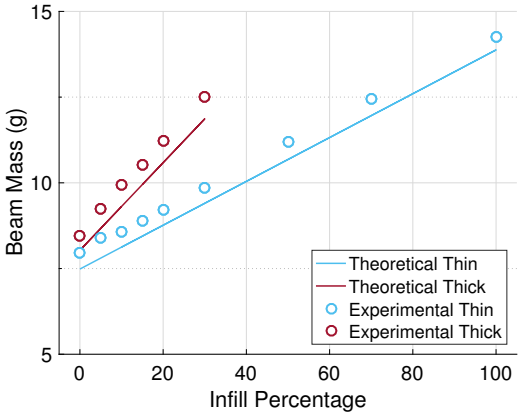

Figure 6: Theoretical and experimental beam masses; $+45°/-45°$ infill orientation.

loads were then compared to estimates calculated with Eq. (7) assuming the flexural rigidity found from the three-point bending tests and the free vibration tests. The assumption of boundary conditions for this calculation (i.e., selection of K) is discussed later (Section 4.6).

4. Results and discussion

4.1. Mass

The mass of each beam was measured with a scale that read to 0.1 mg. The measured masses scaled linearly with infill (see Fig. 6). The theoretical (total) masses were calculated based on the nominal cross section of the specimens and the published density of 1.21 g/cm^3 [23], using Eq. (3) times the printed length. The average measured density based on the measured mass and nominal cross section across all of the beams was 1.27 g/cm^3, but showed some variation with thickness and infill percentage. The differences in masses could be due to the extra material on the ends of the specimens where a sold perimeter is printed or variation in the actual print dimensions.

4.2. Flexural rigidity

Fig. 7 shows the flexural rigidity for the (a) thin beams and (b) thick beams, including the theoretical predictions. Experimental flexural rigidity estimates were obtained for two testing orientations for both the three-point bending and free vibration tests. The flexural

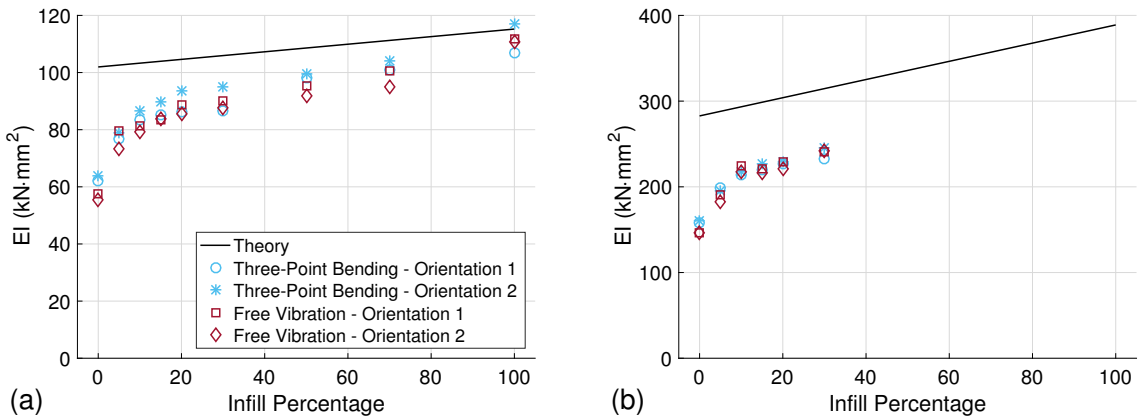

Figure 7: Flexural rigidity of (a) thin and (b) thick beams ($+45°/-45°$ infill orientation) determined from three-point bending tests and free vibration tests.

rigidity is plotted against the infill percentage. The theoretical lines were calculated based on the nominal dimensions of the specimens and Eq. (2). The flexural rigidity of the beams varied fairly linearly with infill percentage except for the lowest infill percentages ($< 10\%$).

The results of the two methods showed good agreement. The stronger orientation of the three-point bending tests were consistently the stiffest (highest EI). The weaker orientation of the free vibration tests was generally the most flexible (smallest EI) of all of the tests. Note that the two orientations for the three-point bending and free vibration tests are not directly comparable because the two orientations represent flipping the specimen around different axes in different test apparatuses.

The theoretical rigidity was consistently higher than the experimental results, but similar trends are observed. The vertical shift in the data is believed to be primarily due to uncertainty in the elastic modulus of the material [23]. As previously noted, the flexural modulus from the manufacturer's data sheet was used for the theoretical calculation, but using the published Young's modulus would have given 20% lower flexural rigidity estimates, matching better the experimental results. Another potential source of discrepancy may be related to the testing apparatuses not perfectly capturing the ideal conditions assumed in theory. For example, the fixity at the clamped end for the free vibration tests was not perfectly fixed, artificially lowering the stiffness.

The slight difference in slope and the convergence of the experiments and theory at 100% infill in Fig. 7(a) could be caused by error in the internal dimensions of the beam; nominal infill properties were assumed for the theoretical calculations. For the free vibration tests, the convergence could also have been caused by the additional solid mass at the end of the beam (note the solid perimeters in Fig. 2).

For the three-point bending tests, the first test orientation consistently produced higher estimates of EI. This could be due to print asymmetries through the beam thickness in combination with compression-tension asymmetry in the FDM PLA [27]. Also, the surface roughness on the first and last layers were different, which could have altered the friction between the specimen and the supports for the two orientations, effecting the boundary conditions. Lastly, the specimens were slightly cambered ($\sim$0.2 mm) due to warping; orientation 1 (2) was cambered up (down), slightly increasing (decreasing) the unsupported length making the beam more flexible (stiff).

For the free vibration tests, the second test orientation generally produced lower estimates of EI. All specimens had the same defect (see Fig. 8) from the printer, which likely contributed to the discrepancy between the two orientations for the specimens. The defect affects the natural frequency through reducing both mass in orientation 1 and stiffness in orientation 2. These two effects compound to lower the natural frequency in the second orientation and therefore the apparent flexural rigidity.

4.3. Specific flexural rigidity

The specific flexural rigidity, or the flexural rigidity EI divided by the length density m, of the specimens was also investigated. Fig. 9 shows the dimensional specific flexural rigidity (EI/m) plotted against infill percentage. The theoretical results were determined using the nominal dimensions of the beam and Eq. (4). As with the flexural rigidity, the experimental specific flexural rigidity values are all lower than the theoretical values. The trend of the experimental specific flexural rigidity values matches the shape of the theoretical specific flexural rigidity for the higher infill percentages ($\geqslant$ 20% for thin beams, $\geqslant$ 10% for thick beams). At lower infill percentages, however, the specific flexural rigidity falls off. The

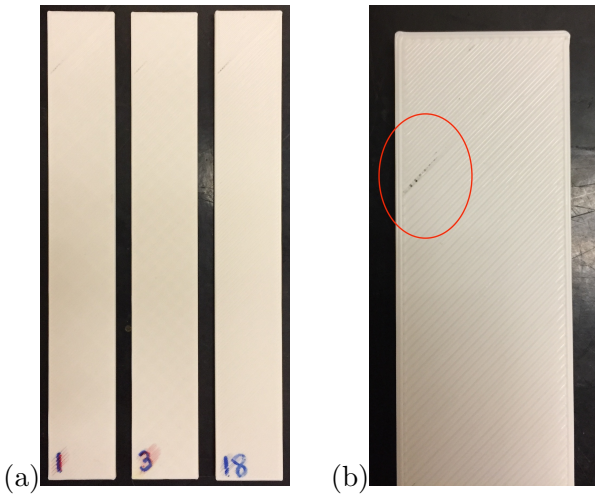

Figure 8: (a) Specimens 1, 3 and 18, which exhibit similar defect; (b) close-up on defect.

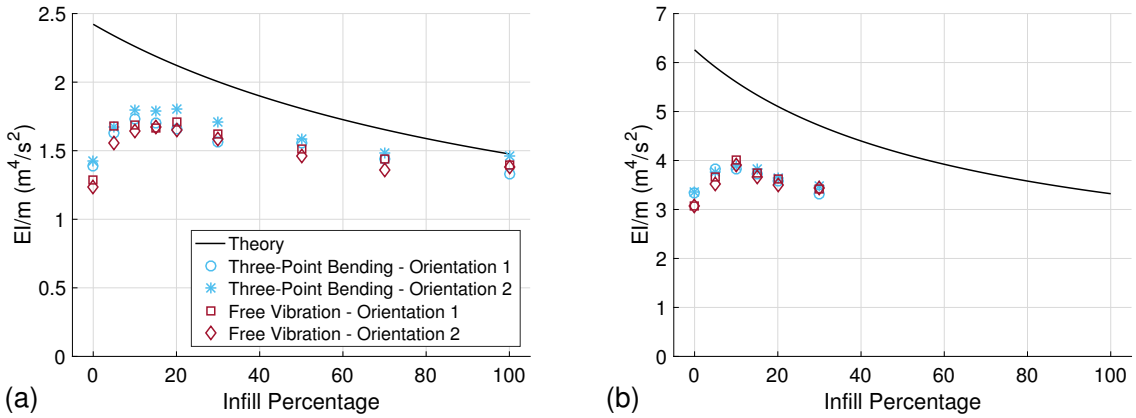

Figure 9: Specific flexural rigidity of (a) thin and (b) thick beams ($+45°/-45°$ infill orientation).

measured mass scaled fairly linearly with the infill percentage (Fig. 6), so the deviation in specific flexural rigidity from theory occurs due to the difference in flexural rigidity (see Fig. 7). The optimal stiffness-to-mass ratio is given by the infill percentage that produces the highest specific flexural rigidity. For the thin beams (Fig. 9(a)), the optimal infill percentage is in the range of 10 to 20%; for the thick beams (Fig. 9(b)), the specific flexural rigidity is highest at 10% infill.

Fig. 10 shows EI/m normalized by the specific flexural rigidity at 0% infill, $(EI/m)_{p=0}$, versus infill percentage. For the experimental results, the value of $(EI/m)_{p=0}$ was determined by fitting a quadratic to the experimental specific flexural rigidity results (Fig. 9). For the

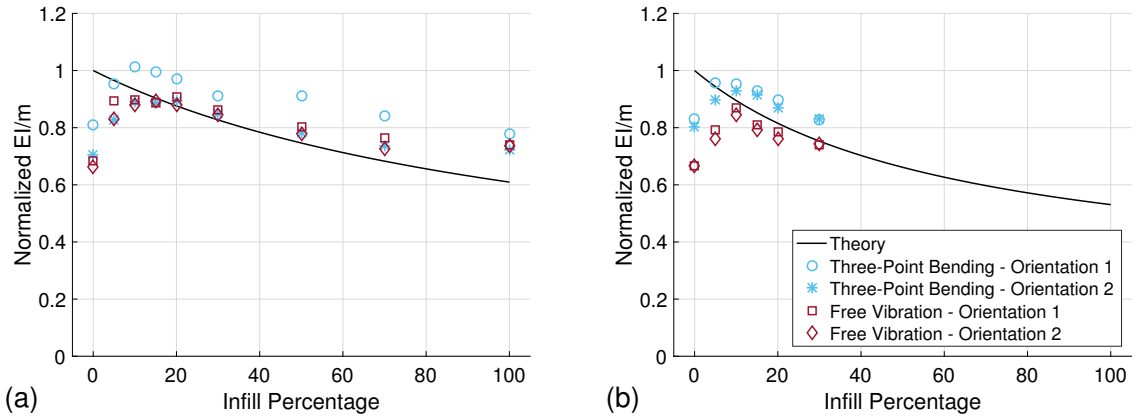

Figure 10: Specific flexural rigidity normalized to 0% infill case and projected 0% infill of (a) thin and (b) thick beams ($+45°/-45°$ infill orientation) determined from three-point bending tests and free vibration tests determined from three-point bending tests and free vibration tests.

thin beams, infill percentages greater than or equal to 20%; for the thick beams, infill percentages greater than or equal to 10% were used to fit the quadratic. The normalized EI/m results (Fig. 10) show better agreement between the theory and experiments for both specimen thicknesses as compared to the dimensional EI/m results (Fig. 9). This is because the normalized EI/m effectively eliminates the influence of the material's elastic modulus E. The specific flexural rigidity of the thin and thick specimens follow different trends on the normalized plot because the effect of specimen thickness is nonlinear (see Eq. (4)) and therefore not removed by normalizing the data.

4.4. Effect of other infill parameters

Fig. 11 shows the flexural rigidity for the thin beams with two different infill orientations versus the infill percentage for the (a) three-point bending tests and (b) free vibration tests. The data for the $0°/90°$ infill orientation falls within the same range as the data for the $+45°/-45°$ infill orientation indicating that the infill orientation has a negligible impact on the flexural rigidity of the specimens. The free vibration results show a tighter grouping with the two infill orientations. When considering only the same test orientation, the three-point bending results were consistent between the two infill orientations. The theoretical flexural rigidity values were calculated based on the nominal dimensions and Eq. (2). The similarity

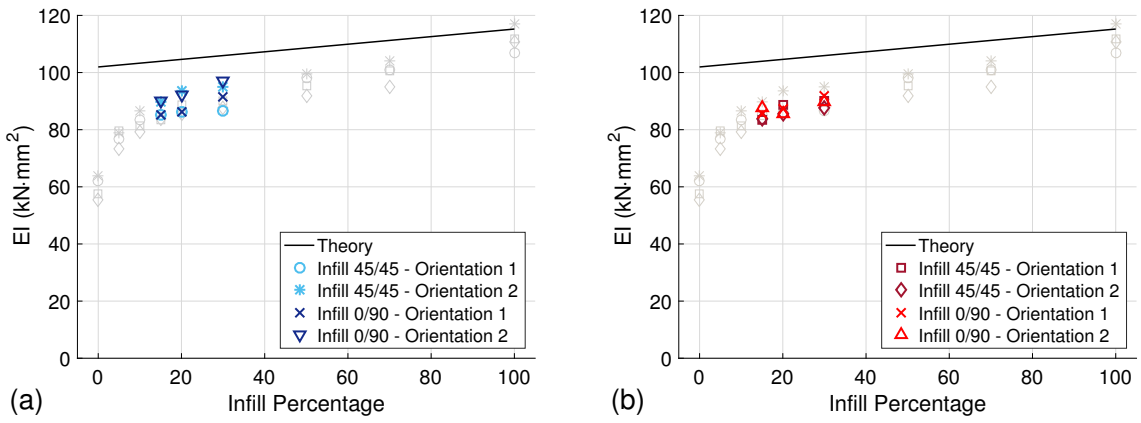

Figure 11: Flexural rigidity for $+45°/-45°$ and $0°/90°$ infill orientations for (a) three-point bending and (b) free vibration. All results for $+45°/-45°$ infill orientation (Fig. 7(a)) are shown in light gray.

in the experimental results with two different infill orientations indicates that a smeared stiffener model [21], as opposed to a discrete stiffener model, is appropriate.

Likewise, the infill orientation had little effect on the specimen masses. The total masses of specimens 2 (12), 3 (13), and 4 (14) were measured to be 8.900 (8.828), 9.225 (9.254), and 9.859 (9.888) g, showing that the masses for the two orientations were fairly consistent.

The 100% infill grid pattern beam (specimen 7) showed higher flexural rigidity than the solid beam (specimen 8); see Table 3. This is partially attributed to specimen 7 being 3.5% thicker than specimen 8. Note, however, that a 3.5% increase in thickness for a (nominally) solid beam should translate to a 11% increase (1.035^3) in flexural rigidity, but only a 5.5% increase in flexural rigidity is realized on average. The full gain in flexural rigidity was not achieved because the 100% infill specimen was not truly solid. Even though specimen 8 was thinner, it weighed 1.7% more than specimen 7, so specimen 7 also had higher specific flexural rigidity; see Table 4. This indicates that a specimen printed with 100% infill has a better stiffness-to-mass ratio than using the solid print setting.

4.5. Discussion of repeatability

For both the three-point bending tests and free vibration tests, specimen 3 was retested an additional five times in each orientation to determine the amount of random deviation in the trials. The mean flexural rigidity (and coefficient of variation) determined from the

five three-point bending tests was 87.1650 kN·mm^2 (0.0280) in orientation 1 and 93.0153 kN·mm^2 (0.0114) in orientation 2; the calculated flexural rigidity of all five trials for each orientation fell within 3.5% of the mean. The mean flexural rigidity (and coefficient of variation) determined from the five free vibration tests was 90.3835 kN·mm^2 (0.0198) in orientation 1 and 85.9433 kN·mm^2 (0.0183) in orientation 2; the calculated flexural rigidity of all five trials for each orientation fell within 2.2% of the mean. The low coefficients of variation indicate that the testing of a specimen is repeatable for a given orientation. The orientation, however, had a non-negligible influence on the determined flexural rigidity, as previously discussed.

The four duplicate specimen 3 (specimens 3b–3e) were fabricated and tested to assess the repeatability of the 3D printing process. The mean flexural rigidity (and coefficient of variation) for these four specimen were determined from three-point bending tests to be 86.7207 kN·mm^2 (0.0279) in orientation 1 and 91.0487 kN·mm^2 (0.0150) in orientation 2 and from free vibration tests to be 88.5343 kN·mm^2 (0.0197) in orientation 1 and 83.8914

Table 3: Flexural rigidity of 100% infill and solid specimens.

Specimen No.	EI (kN·mm^2)			
	Three-Point Bending		Free Vibration	
	Orientation 1	Orientation 2	Orientation 1	Orientation 2
7	106.7	117.0	111.7	110.7
8	101.2	112.4	108.0	101.7

Table 4: Specific flexural rigidity of 100% infill and solid specimens.

Specimen No.	EI/m (m^4/s^2)			
	Three-Point Bending		Free Vibration	
	Orientation 1	Orientation 2	Orientation 1	Orientation 2
7	1.332	1.461	1.394	1.382
8	1.243	1.380	1.326	1.248

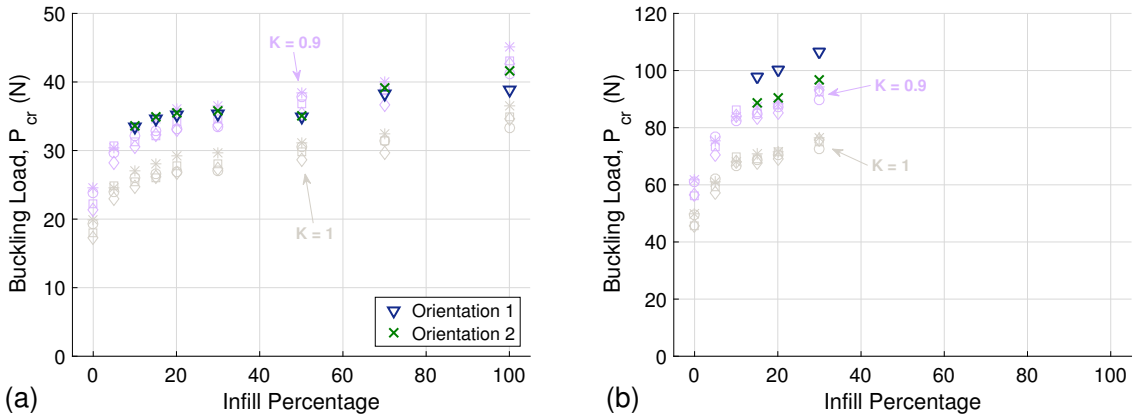

Figure 12: Buckling load P_{cr} of (a) thin and (b) thick beams ($+45°/-45°$ infill orientation) determined from buckling tests in orientations 1 and 2. Predicted P_{cr} using Eq. (7) based on flexural rigidities determined from three-point bending and free vibration tests (Fig. 7) for effective length factors $K = 1$ (pinned) and $K = 0.9$ (semi-rigid) are shown for comparison.

kN·mm^2 (0.0189) in orientation 2. For all of the prints of specimen 3 (specimens 3 and 3b–3e), the flexural rigidity was within 3.9% for the three-point bending tests and 3.4% for the free vibration tests of the mean for a given orientation. The mean flexural rigidity for specimens 3b–3e is lower than the flexural rigidity of specimen 3 in all test configurations. This may be due to aging effects [28] resulting from inconsistent time between fabrication and testing for specimen 3 and specimens 3b–3e; specimens 3b–3e were printed in succession and tested the next day, whereas specimen 3 had been printed approximately 6 weeks prior. This aging effect, however, was less influential than the testing orientation for both test methods.

4.6. Buckling results

As previously noted, the buckling tests were used to confirm the results of the three-point bending tests and free vibration tests. Fig. 12 shows the critical buckling load determined from the buckling tests. The experimentally determined P_{cr} are superimposed on estimates based on Eq. (7) assuming the flexural rigidity values found from the three-point bending and free vibration tests (Fig. 7). Two values for the effective length factor were used in evaluating Eq. (7): $K = 1.0$ (pinned) and 0.9 (semi-rigid). Assuming pinned boundary

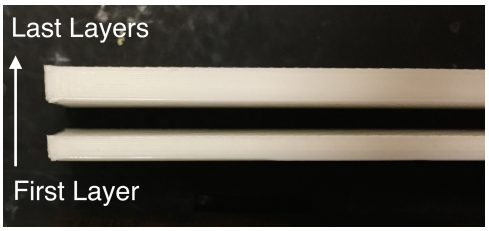

Figure 13: Edge view of thin and thick beams showing non-square edges due to warping (shortening) of first layer.

conditions ($K = 1$), the measured buckling loads overestimate the values predicted based on the other two test methods. While the buckling test setup (Fig. 5(a)) was designed to mimic pinned connections, perfect (frictionless) pin connections cannot be achieved experimentally. Taking $K = 0.9$, a better match to the three-point bending and free vibration test data is observed.

Less variability with test orientation was observed for the thin beams (Fig. 12(a)) than for the thick beams (Fig. 12(b)). This may be attributed to the edges of the beam not being perfectly square due to warping (see Fig. 13); the specimen were slightly shorter on the side in contact with the print bed (first layer), which produced a load eccentricity on the specimens through the longer edge (last layer). This eccentricity was larger for the thick beams having a more significant effect on the experimentally determined buckling loads.

To assess the repeatability of the buckling tests, specimen 3 was tested five times; the corresponding load-deflection curves are shown in Fig. 5(b). Note that, while the load path varied with specimen orientation, the estimated buckling load (determined at 1.5 mm of end shortening) was repeatable; the mean buckling load (and coefficient of variation) for the five tests in orientations 1 and 2 were 36.2 N (0.0039) and 35.7 N (0.0049), respectively. Similar to the other test methods, the four duplicate specimen 3 (specimens 3b–3e) were tested five times as well to characterize the repeatability of the 3D printing process. Fig. 14 show the compressive load-deflection curves for all fifty buckling tests of these nominally identical specimens and orientations. The mean estimated buckling load for all fifty tests is 34.9 N with a coefficient of variation of only 0.0208, indicating a high level of repeatability.

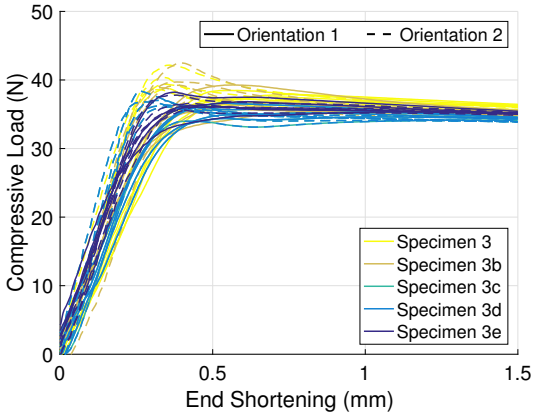

Figure 14: Repeatability of buckling tests: Compressive load versus end shortening curves for specimens 3, 3b, 3c, 3d, and 3e in orientations 1 and 2.

5. Concluding remarks

3D-printed cellular structures have the potential to increase the efficiency of load-bearing structural members, conserving material without much loss of stiffness. The objective of this study was to investigate the impact of key infill parameters—percentage and orientation—on the flexural properties of PLA specimens built on a consumer-grade 3D printer (Lulzbot Taz 6). This paper compared and contrasted flexural properties—flexural rigidity EI and specific flexural rigidity EI/m—determined from three-point bending tests and free vibration tests, as well as buckling tests for validation. Based on the results, the optimal infill percentage for maximizing the stiffness-to-mass of 3D-printed structural members is around 10 to 20%. However, it is recommended to use a slightly higher infill in order to safely avoid the drop off in flexural rigidity at the lowest infill percentages. The infill orientation had a negligible effect on the experimentally determined flexural rigidity, indicating that a smeared stiffener approach used to predict the second moment of area (I) is reasonable. However, the results also indicated that the smeared stiffener approach is not effective at the lowest infill percentages. Given the uncertainty in elastic modulus (E) for 3D printed structures, care should be taken in comparing theoretical calculations and experimental results. Better agreement between theory and experiment was observed when the effect of E was eliminated (through normalization). This study considered only bending about the weak axis perpen-

dicular to the build direction. The results are not directly applicable to bending around the vertical print axis because, at lower infill percentages, the second moment of area about the vertical axis varies significantly along the length of the beam.

Acknowledgement

This material is based upon work supported by the National Science Foundation under Grant No. NSF-CMMI-1663376. This support is greatly appreciated. Financial support through the Undergraduate Research Opportunities Program (UROP) from the Honors College at the University of Oklahoma is also acknowledged. Finally, the authors thank Rachel C. Childers and the Stephenson School of Biomedical Engineering for providing access to the universal testing machine used in this research.

References

[1] T. A. Schaedler, W. B. Carter, Architected Cellular Materials, Annual Review of Materials Research 46 (1) (2016) 187–210, doi:10.1146/annurev-matsci-070115-031624.

[2] Y.-T. Kao, Y. Zhang, J. Wang, B. L. Tai, Bending behaviors of 3D-printed Bi-material structure: Experimental study and finite element analysis, Additive Manufacturing 16 (2017) 197–205, doi:10.1016/j.addma.2017.06.005.

[3] O. Lužanin, D. Movrin, M. Plančak, Effect of layer thickness, deposition angle, and infill on maximum flexural force in FDM-built specimens, Journal for Technology of Plasticity 39 (1) (2014) 49–57.

[4] J.-P. Kruth, M. Leu, T. Nakagawa, Progress in Additive Manufacturing and Rapid Prototyping, CIRP Annals 47 (2) (1998) 525–540, ISSN 0007-8506, doi:10.1016/S0007-8506(07)63240-5.

[5] M. I. Mohammed, B. Cadd, G. Peart, I. Gibson, Augmented patient-specific facial prosthesis production using medical imaging modelling and 3D printing technologies for improved patient outcomes, Virtual and Physical Prototyping 13 (3) (2018) 164–176, doi:10.1080/17452759.2018.1446122.

[6] R. K. Chen, Y. an Jin, J. Wensman, A. Shih, Additive manufacturing of custom orthoses and prostheses a review, Additive Manufacturing 12 (2016) 77–89, doi:10.1016/j.addma.2016.04.002.

[7] S. Ravindrababu, Y. Govdeli, Z. W. Wong, E. Kayacan, Evaluation of the influence of build and print orientations of unmanned aerial vehicle parts fabricated using fused deposition modeling process, Journal of Manufacturing Processes 34 (2018) 659–666, doi:10.1016/j.jmapro.2018.07.007.

[8] N. Mohan, P. Senthil, S. Vinodh, N. Jayanth, A review on composite materials and process parameters optimisation for the fused deposition modelling process, Virtual and Physical Prototyping 12 (1) (2017) 47–59, doi:10.1080/17452759.2016.1274490.

[9] J. R. C. Dizon, A. H. Espera, Q. Chen, R. C. Advincula, Mechanical characterization of 3D-printed polymers, Additive Manufacturing 20 (2018) 44–67, doi:10.1016/j.addma.2017.12.002.

[10] D. Popescu, A. Zapciu, C. Amza, F. Baciu, R. Marinescu, FDM process parameters influence over the mechanical properties of polymer specimens: A review, Polymer Testing 69 (2018) 157–166, doi:10.1016/j.polymertesting.2018.05.020.

[11] X. Zhou, S.-J. Hsieh, C.-C. Ting, Modelling and estimation of tensile behaviour of polylactic acid parts manufactured by fused deposition modelling using finite element analysis and knowledge-based library, Virtual and Physical Prototyping 13 (3) (2018) 177–190, doi:10.1080/17452759.2018.1442681.

[12] P. K. Gurrala, S. P. Regalla, Multi-objective optimisation of strength and volumetric shrinkage of FDM parts, Virtual and Physical Prototyping 9 (2) (2014) 127–138, doi:10.1080/17452759.2014.898851.

[13] W. C. Smith, R. W. Dean, Structural characteristics of fused deposition modeling polycarbonate material, Polymer Testing 32 (8) (2013) 1306 – 1312, doi:10.1016/j.polymertesting.2013.07.014.

[14] B. Wittbrodt, J. M. Pearce, The effects of PLA color on material properties of 3-D printed components, Additive Manufacturing 8 (2015) 110 – 116, ISSN 2214-8604, doi:10.1016/j.addma.2015.09.006.

[15] J. Chacón, M. Caminero, E. Garc´infilla-Plaza, P. Núñez, Additive manufacturing of PLA structures using fused deposition modelling: Effect of process parameters on mechanical properties and their optimal selection, Materials & Design 124 (2017) 143 – 157, ISSN 0264-1275, doi:10.1016/j.matdes.2017.03.065.

[16] L. N. Virgin, On the flexural stiffness of 3D printer thermoplastic, International Journal of Mechanical Engineering Education 45 (1) (2017) 59–75, doi:10.1177/0306419016674140.

[17] K. P. Motaparti, G. Taylor, M. C. Leu, K. Chandrashekhara, J. Castle, M. Matlack, Experimental investigation of effects of build parameters on flexural properties in fused deposition modelling parts, Virtual and Physical Prototyping 12 (3) (2017) 207–220, doi:10.1080/17452759.2017.1314117.

[18] K. L. Alvarez, C., R. F. Lagos, C., M. Aizpun, Investigating the influence of infill percentage on the mechanical properties of fused deposition modelled ABS parts, Ingenier´infilla e Investigación 36 (3) (2016) 110–116, doi:10.15446/ing.investig.v36n3.56610.

[19] L. N. Virgin, Enhancing the teaching of linear structural analysis using additive manufacturing, Engineering Structures 150 (Supplement C) (2017) 135–142, doi:10.1016/j.engstruct.2017.07.054.

[20] L. N. Virgin, Enhancing the teaching of structural dynamics using additive manufacturing, Engineering Structures 152 (Supplement C) (2017) 750–757, ISSN 0141-0296, doi:10.1016/j.engstruct.2017.09.052.

[21] D. H. Bich, D. V. Dung, V. H. Nam, Nonlinear dynamical analysis of eccentrically stiffened functionally

graded cylindrical panels, Composite Structures 94 (8) (2012) 2465–2473, doi:10.1016/j.compstruct.2012.03.012.

[22] P. S. Harvey, L. N. Virgin, Effect of Stiffener Geometry on the Response of Grid-Stiffened Panels, Journal of Engineering Mechanics 144 (2) (2018) 06017021, doi:10.1061/(ASCE)EM.1943-7889.0001415.

[23] PolyLite^{TM} PLA Technical Data Sheet, Polymaker, 2017.

[24] ASTM D790, Standard Test Methods for Flexural Properties of Unreinforced and Reinforced Plastics and Electrical Insulating Materials, doi:10.1520/D0790-10, West Conshohocken, PA, 2010.

[25] ASTM E1876, Standard Test Method for Dynamic Young's Modulus, Shear Modulus, and Poisson's Ratio by Impulse Excitation of Vibration, doi:10.1520/E1876-15, West Conshohocken, PA, 2015.

[26] M. Gasior, J. L. Gonzalez, Improving FFT Frequency Measurement Resolution by Parabolic and Gaussian Spectrum Interpolation, AIP Conference Proceedings 732 (1) (2004) 276–285, doi:10.1063/1.1831158.

[27] C. Perkowski, Tensile-Compressive Asymmetry and Anisotropy of Fused Deposition Modeling PLA under Monotonic Conditions, Master's thesis, University of Central Florida, Orlando, FL, 2017.

[28] J. Mueller, S. E. Kim, K. Shea, C. Daraio, Tensile properties of inkjet 3d printed parts: critical process parameters and their efficient analysis, in: Proceedings of the ASME 2015 International Design Engineering Technical Conferences & Computers and Information in Engineering Conference IDETC/CIE 2015, Boston, Massachusetts, USA, 2015.